https://doi.org/10.15407/ujpe70.10.717

O.S. PYLYPCHUK,[1] V.O. KOLUPAIEV,[1] I.V. FESYCH,[2] V.N. POROSHIN,[1]
A.N. MOROZOVSKA [1]

[1] Institute of Physics, Nat. Acad. of Sci. of Ukraine
(46, Nauky Ave, Kyiv 03028, Ukraine)
[2] Taras Shevchenko National University of Kyiv
(64/13, Volodymyrska Str., Kyiv 01601, Ukraine)

INVESTIGATION OF ELECTROPHYSICAL PROPERTIES, PHASE DIAGRAMS, AND CHARGE CARRIER TRANSFER IN $\mathbf{Bi_{1-x}Sm_xFeO_3}$

Nanoscale multiferroics with different sizes and shape parameters are basic model objects for studying polar, antipolar, and magnetic orientation, as well as magnetoelectric interaction. Bismuth–Samarium oxide ($Bi_{1-x}Sm_xFeO_3$) is a classical orthoferrite, whose polar and magnetic properties have been sufficiently studied for the bulk and thin film samples. However, the properties of $Bi_{1-x}Sm_xFeO_3$ nanoparticles have been studied much less theoretically and experimentally, even though they can be used for the energy harvesting and storage, as well as for creating advanced FeRAM devices. In this work, we use the Ginzburg–Landau–Devonshire approach to perform phenomenological calculations of polar and dielectric properties of $Bi_{1-x}Sm_xFeO_3$ nanoparticles, and construct phase diagrams in dependence on the nanoparticle average size, and on the proportion of samarium in solid solution. Calculations of the surface adsorption/desorption influence on dielectric, polar and magnetoelectric properties at different temperatures are performed in the framework of the Stephenson–Highland approach. Experimental studies of the frequency dependence of the $Bi_{1-x}Sm_xFeO_3$ nanopowders dielectric susceptibility and conductivity are carried out. The experimental results correlate with theoretical predictions, which allows us to improve the understanding of the physical mechanisms of conductivity and charge transfer in orthoferrite nanopowders, which will further allow us to create new nanocompounds with improved and/or controllable properties, as well as expand the perspectives of their advanced applications in nanoelectronics and energy storage.

Keywords: multiferroics, nanoparticles, dielectric susceptibility, conductivity, phase diagrams.

1. Introduction

Multiferroic materials, which exhibit simultaneous ferroelectric and magnetic ordering, have gained considerable attention due to their potential applications in spintronic devices, sensors, memory devices, and energy harvesting systems. Bismuth ferrite ($BiFeO_3$) is one of the few single-phase multiferroic materials that exhibit both ferroelectricity and antiferromagnetism at room temperature. However, pure $BiFeO_3$ has limitations such as a high leakage current, helically modulated spin structure, and phase instability. One approach to overcome these problems is the addition of another elements, in particular the rare earth ones, such as samarium (Sm) [1–2].

Nanoscale multiferroics with different sizes and shape parameters are basic model objects for studying the polar, antipolar, and magnetic orientation as well as magnetoelectric interaction. Bismuth–Samarium oxide ($Bi_{1-x}Sm_xFeO_3$) is a classical orthoferrite, whose polar and magnetic properties have been sufficiently studied for the bulk and thin film samples. However, the properties of $Bi_{1-x}Sm_xFeO_3$ nanoparticles have been studied much less theoretically and exper-

---

Citation: Pylypchuk O.S., Kolupaiev V.O., Fesych I.V., Poroshin V.N., Morozovska A.N. Investigation of electrophysical properties, phase diagrams and charge carrier transfer in $Bi_{1-x}Sm_xFeO_3$. *Ukr. J. Phys.* **70**, No. 10, 717 (2025). https://doi.org/10.15407/ujpe70.10.717.

imentally [3], even though they can be used for the energy harvesting [4] and storage [5], as well as for creating advanced FeRAM devices [6].

Therefore, the electrophysical and magnetic properties of bismuth orthoferrites with addition of samarium ($Bi_{1-x}Sm_xFeO_3$) ($B_{1-x}Sm_xFe_3$) particles, which have more stable properties, are of research interest. The following review summarizes the main research results related to the synthesis, structural, electrical, magnetic, and optical properties of $Bi_{1-x}Sm_xFeO_3$, and discusses how the Sm substitution improves the characteristics of $BiFeO_3$.

$BiFeO_3$ has a rhombohedral deformed structure of perovskite (space group *R3c*) at room temperature. The addition of samarium ions in $BiFeO_3$ leads to a noticeable structural changes. Sm^{3+} ions have a smaller ionic radius (1.08 Å) compared to Bi^{3+} (1.17 Å), which leads to lattice deformation [7].

Several studies have reported the presence of a phase transition from the rhombohedral (*R3c*) to orthorhombic (*Pnma*) symmetry with increasing Sm content ($x > 0.15\div0.20$). For example, observed this transition at $x = 0.20$, which was confirmed by the XRD and the Raman scopy [8]. Such structural transitions are associated with a changes in lattice parameters, unit cell volume, and tolerance coefficient. The main phase and structural features are as follows: an increase in the Sm content stabilizes the orthorhombic phase [9], lattice deformation and nanoparticle size decrease with an increase in the Sm content [10], and phase coexistence can occur in the intermediate interval of $x = 0.10\div0.20$) [11].

$BiFeO_3$ high ferroelectric polarization ($\sim100\,\mu C/cm^2$) is often accompanied by the high leakage currents due to oxygen vacancies and Bi volatility. The addtion of Sm improves ferroelectric properties by reducing the oxygen vacancy concentration and increasing the grain boundary resistance of nanoparticle interfaces. Zhang *et al.* observed that the optimal Sm content levels ($x \approx 0.10\div0.20$) lead to an increased dielectric constants and reduced dielectric losses [1]. Enhanced ferroelectric (P-E) hysteresis loops with higher remanent polarization and lower coercive fields have been reported in this interval of x. The main magnetic features are: magnetic transition from the antiferromagnetic to a weak ferromagnetic state, an increase in the saturation magnetization, when the Sm content level is approaching the optimum concentration, when the optimum Sm content level is exceeded, the magnetization decreases due to the formation of secondary phases or reduction of the magnetic interactions [12].

The addition of samarium also affects the optical band gap of $BiFeO_3$. Due to the lattice deformation and a changes in Fe–O–Fe bond angles, the band gap tends to increase slightly with Sm substitution. UV-Vis spectroscopy reveals a shift in the absorption edge, indicating a changes in the optical band gap. For example, reported an increase in the band gap from 2.15 eV (pure $BiFeO_3$) to 2.30 eV ($x = 0.20$), which could be beneficial for photocatalytic and optoelectronic applications The main optical features are: the band gap increases with the addition of Sm ions, the optical absorption limit shifts toward shorter wavelengths, it's useful for adapting materials for applications operating in visible light [8, 13].

Studies of the electrical conductivity show that Sm ions reduce the conductivity and increases the activation energy, which is associated with a decrease in the number of oxygen vacancies [14]. Impedance spectroscopy reveals an improvement in the resistance at the particle boundary and a decrease in dielectric losses. The mechanism of conductivity in many cases corresponds to the model of a small polaron jump [15].

Electrical conductivity studies show that the addition of Sm reduces the conductivity and increases the activation energy, which is associated with a decrease in the number of oxygen vacancies. Impedance spectroscopy reveals an improvement in grain boundary resistance and a decrease in dielectric losses. The mechanism of conductivity in many cases corresponds to the small polaron jump model. Main electrophysical features: increased the resistivity and reduced the leakage current, improved electrical insulation characteristics, presence of a jump conduction mechanism [15].

Common methods for the synthesis of $Bi_{1-x}Sm_xFeO_3$ include:

- sol-gel method: Provides a better stoichiometric control and homogeneity [2];
- reaction in the solid state: simpler, but can lead to the formation of larger particles and, secondary phases [1];
- hydrothermal synthesis: allows one to obtain well-crystallized nanoparticles [16];
- pulsed Laser Deposition [17].

Annealing and sintering parameters significantly affect phase purity, nanoparticle growth, and functional properties. Due to its improved multiferroic, magnetic, and optical properties, $Bi_{1-x}Sm_xFeO_3$ has potential applications in: non-volatile memory devices, spintronics, magnetic sensors, and actuators, visible light photocatalysis, and dielectric capacitors with high permittivity [18–22].

$Bi_{1-x}Sm_xFeO_3$ orthoferrites are a promising class of modified multiferroics. The substitution of Sm^{3+} improves the magnetic, dielectric, and ferroelectric properties of BiFeO3 by changing its structure and reducing internal defects. The optimal content of Sm is $x \approx 0.10 \div 0.20$ provides a significant improvement in properties. For practical applications, further studies of thin films, composites, and device integration are needed. In particular, complex composites, which contain $Bi_{1-x}Sm_xFeO_3$ nanoparticles and metallic nanoparticles placed in dielectric matrix, can become very promising for photogeneration of sound [23], light scattering [24], electron-lattice energy exchange [25], and non-local effects [26] in metal nanoparticles.

In this work, we will use the Ginzburg–Landau–Devonshire (LGD) approach to perform phenomenological calculations of polar and dielectric properties of $Bi_{1-x}Sm_xFeO_3$ nanoparticles, and construct phase diagrams in dependence on the nanoparticle sizes and shape parameters, and on the proportion of samarium in solid solution. Calculations of the surface adsorption/desorption influence on the dielectric, polar, and magnetoelectric properties at different temperatures are performed in the framework of the Stephenson-Highland (SH) approach.

Experimental studies of the frequency dependences of the $Bi_{1-x}Sm_xFeO_3$ nanopowders dielectric permittivity and the conductivity are performed. The results of the study will allow one to improve the understanding of the physical mechanisms of conductivity and charge transfer in orthoferrite nanopowders, which will further allow us to create new nanocompounds with improved and/or controllable properties, as well as expand the perspectives of their advanced applications in nanoelectronics and energy storage.

2. Theoretical Modelling

The free energy of a homogeneous bulk $Bi_{1-x}Sm_xFeO_3$ in the dimensionless form is as follows [3]:

$$F_{\text{bulk}} = \frac{1}{2}\eta\left(T,x\right)A^2 + \frac{1}{2}\alpha\left(T,x\right)P^2 + \frac{1}{4}\beta_{ij}\left(P_i^2P_j^2 + \right.$$
$$\left. + A_i^2A_j^2\right) + \frac{1}{2}\xi_{ij}P_i^2A_j^2 - \mathbf{PE}. \tag{1}$$

The functions $\alpha\left(T,x\right)$ and $\eta\left(T,x\right)$ are dimensionless temperature and chemical composition dependent functions [3]:

$$\begin{aligned} &\alpha\left(T,x\right) = \frac{T}{T_{\text{C}}} - \exp\left[-\left(\frac{x}{x_c}\right)^4\right], \\ &\eta\left(T,x\right) = \eta_0\left\{\frac{T}{T_A} - \exp\left[-\left(\frac{x}{x_A}\right)^2\right]\right\}, \end{aligned} \tag{2}$$

Here, T is the temperature, x is the content of samarium, T_c is the Curie temperature, x_c is the proportion of samarium at which the phase transition from the ferroelectric (FE) phase to the nonpolar (NP) phase occurs, T_A is the Neel temperature, x_A is the proportion of samarium at which the phase transition from the antiferroelectric (AFE) phase to the NP phase occurs, η_0 is a dimensionless coefficient corresponding to the relative amplitude of the AFE mode. $\mathbf{P} = (P_1,\, P_2,\, P_3)$ and $\mathbf{A} = (A_1,\, A_2A_3)$ are polar and antipolar dimensionless vectors, respectively. The NP phase is stable at high x.

The free energy functional F of $Bi_{1-x}Sm_xFeO_3$ nanoparticles without mechanical stress using the Four Sublattice Model (FSM), the Landau–Ginsburg–Devonshire–Kittel (LGDK) and Stevenson–Highland (SH) approaches [27]:

$$F = F_{\text{bulk}} + F_{\text{grad}} + F_{\text{el+fl}} + F_{\text{el}} + F_{\text{s}}. \tag{3}$$

The component F_{bulk} is the bulk fraction; F_{grad} is the polarization gradient energy; $F_{\text{el+fl}}$ is the elastic and flexoelectric energy; F_{el} is the electrostatic energy; F_{s} is the surface energy, which are listed in Appendix A.

For ellipsoidal nanoparticles, the dependence of α on the particle sizes is as follows [3]:

$$\frac{\alpha_R\left(T,x,R\right)}{\alpha_0} = \frac{T}{T_{\text{C}}} - \exp\left[-\left(\frac{x}{x_{\text{C}}}\right)^4\right] +$$
$$+ \frac{1}{\varepsilon_0\alpha_0}\frac{n_d}{\varepsilon_b n_d + \varepsilon_M\left(1-n_d\right) + \varepsilon_s n_d\left(D/\lambda\right)}. \tag{4}$$

Here, ε_b and ε_e are the dielectric permittivity of ferroelectric background [28] and external media respectively, $n_d = \frac{1-\xi^2}{\xi^3}\left(\ln\sqrt{\frac{1+\xi}{1-\xi}} - \xi\right)$ is the depolarization factor, $\xi = \sqrt{1-(R/L)^2}$ is the eccentricity ratio of ellipsoid with a shorter semi-axes R and longer semi-axis L, and D is the ellipsoid semi-axis (R or L) in the direction of spontaneous polarization P_3 and λ is the screening length [29]. The derivation of Eq. (4) is given in Ref. [30]. To focus on the external pressure effect, we neglect the surface tension and polarization gradient effects considered elsewhere [31–33].

Within the SH-model, the dependence of the surface charge density $\sigma_s[\phi]$ on the excess electric potential $\delta\phi$ on the surface of the nanoparticle is controlled by the concentration of positive and negative surface charges in a self-consistent manner. The density $\sigma_s[\phi]$ obeys the Langmuir adsorption isotherm [3]:

$$\sigma_{\mathrm{s}}[\phi] = \sum_{i=1}^{2} \frac{eZ_i\theta_i[\phi]}{N_i} \cong$$
$$\cong \sum_{i=1}^{2} \frac{eZ_i}{N_i}\left(1+\exp\left[\frac{\Delta G_i + eZ_i\delta\phi}{k_{\mathrm{B}}T}\right]\right)^{-1}. \quad (5)$$

Here, e is the electron charge, $Z_i$is the ionization number of surface ions/vacancies, T is the absolute temperature, $n_i = 1/N_i$ is the charge density, and ΔG_i is the energy of formation of surface charges under normal conditions. It is reasonable to assume that $\varepsilon_M \approx \varepsilon_s$ for ultrathin shells consisting of an ionic-electronic charge absorbed from the environment.

Linearization of the expression in Eq. (5) for small built-in potentials $\left|\frac{eZ_i\delta\phi}{k_{\mathrm{B}}T}\right| < 1$ leads to an approximate expression for the effective surface charge density σ_s and the inverse screening length $1/\lambda$:

$$\sigma_s[\phi] \approx -\varepsilon_0\frac{\delta\phi}{\lambda}, \quad \frac{1}{\lambda} \approx \sum\nolimits_i \frac{(eZ_i)^2 n_i}{4\varepsilon_0 k_{\mathrm{B}}T\cosh^2\left(\frac{\Delta G_i}{2k_{\mathrm{B}}T}\right)}. \quad (6)$$

Substitution of Eq. (6) into Eq. (4) leads to the following renormalization of the dimensionless coefficient $\alpha(T, x)$ in Eq. (2):

$$\alpha_R(T, x, R) = \frac{T}{T_c} - \exp\left[-\left(\frac{x}{x_c}\right)^4\right] +$$
$$+ \frac{(\alpha_0\varepsilon_0)^{-1} n_d}{\varepsilon_b n_d + \varepsilon_M(1-n_d) + \varepsilon_{\mathrm{s}} n_d (D/\lambda)}. \quad (7)$$

The free energy with the renormalized coefficient $\alpha_R(T, x, R)$ allows us to describe analytically the size effects and the influence of ferroionic bonding on the phase diagrams and polar properties of single-domain $\mathrm{Bi}_{1-x}\mathrm{Sm}_x\mathrm{FeO}_3$ nanoparticles.

The dimensionless dielectric constant $\chi_{33}$is defined by the equation [3]

$$\chi_{33} = \frac{\partial P_3}{\partial E_3} =$$
$$= \frac{\eta + 3\beta A_3^2 + \xi P_3^2}{(\alpha_R + 3P_3^2 + \xi A_3^2)(\eta + 3\beta A_3^2 + \xi P_3^2) - 4\xi^2 P_3^2 A_3^2}. \quad (8)$$

The reentrant transition between the ferrielectric (FEI) and ferroelectric (FE) phases exists for the average radius $R > R_R$ as shown in Fig. 1, *a*. Here, we assume averaging over the particles size anisotropy and regard that R is the average particle size hereinafter. The influence of R on the transition from the FEI to the AFE phase is much weaker; and the influence of R on the AFE-NP transition is absent, because the depolarization field is absent in the homogeneous AFE and NP phases [3].

Dependencies of the spontaneous polarization P_S and antipolar parameter A_S on the Sm content x and the average radius R are shown in Fig. 1, *b* and Fig. 1, *c*, respectively. The spontaneous polarization relatively weakly depends on R. Here, it is maximal at $x = 0$, decreases monotonically with x increase and vanishes at $x \geq x_{\mathrm{cr}}(R)$, where $x_{\mathrm{cr}}(R) \approx 0.1$ for $R > 8$ nm. The spontaneous antipolar order exists in the FEI and AFE phases. It gradually disappears approaching the FEI-FE boundary, as well as it disappears approaching the AFE-NP boundary (which is close to the vertical line $x \approx 0.15$). The antipolar order reaches maximal values at the FEI-AFE boundary.

The dependences of the nanoparticle static dielectric susceptibility χ on the Sm content x was calculated in zero electric field ($E \to 0$) for several values of the nanoparticle radius from 4 nm to 80 nm. The dependences are shown in Fig. 1, *d*. The susceptibility diverges at the critical value $x = x_{\mathrm{cr}}$, and x_{cr} increases with increase in R (compare different curves in Fig. 1, *d*). The divergency corresponds to the second order transition between the FEI and AFE phases. For average radii $R < R_R$ any features of the reentrant FE-FEI transition are not visible at the dielectric susceptibility curve, because the transition is absent for the radii interval in Fig. 1, *a*. Since the strength ξ of the biquadratic coupling is very small,

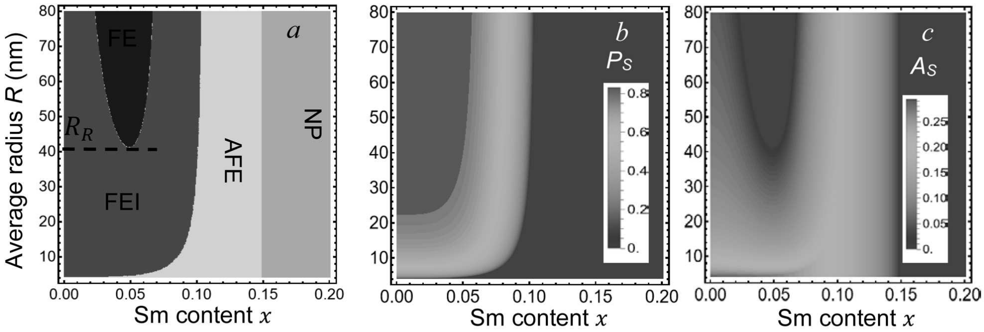

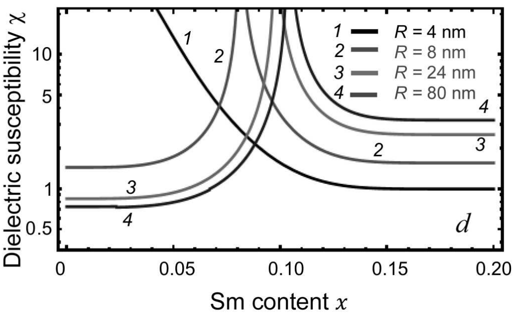

Fig. 1. The phase diagram of $\mathrm{Bi}_{1-x}\mathrm{Sm}_x\mathrm{FeO}_3$ nanoparticles in dependence on the Sm content x and the particle average radius R (a). Dependencies of the spontaneous polarization P_S (b) and antipolar order A_S (c) on the x and R. The dependence of the nanoparticle dielectric susceptibility on the Sm content x calculated at $E = 0$ for average radius $R = 4$ nm (curve (*1*)), 8 nm (curve (*2*)), 24 nm (curve (*3*)) and 80 nm (curve (*4*)). The temperature $T = 25$ °C, $\varepsilon_M = 12$; other parameters are listed in Ref. [3] (d)

the appearance and changes of the antipolar order cannot change the static dielectric susceptibility χ in a noticeable way.

According to theoretical predictions, the static dielectric permittivity of pure BiFeO_3 is maximal at small nanoparticle radii (4 nm and less) and monotonically decreases with ncreasiing the Sm content up to 20% (see the black curve in Fig. 1, *d*). When the particle radius increases above the critical value, a sharp maximum appears at the critical samarium content $x_{cr}(R)$ and the monotonic behavior of the curves with content x is violated (see colored curves in Fig. 1, *d*). In this case, the smallest permittivity corresponds to 80-nm BiFeO_3 nanoparticles (below $x_{\mathrm{cr}}(R)$), and it becomes the highest above $x_{\mathrm{cr}}(R)$. The largest permittivity corresponds to 8-nm BiFeO_3 nanoparticles (below $x_{\mathrm{cr}}(R)$), and it becomes the smallest above x_{cr}.

In the next section, we will demonstrate that this behavior of permittivity, predicted theoretically, qualitatively correlates with experimental measurements of the dielectric permittivity of the pressed $\mathrm{Bi}_{1-x}\mathrm{Sm}_x\mathrm{FeO}_3$ nanopowders. However, since the theoretical results were obtained for spherical nanoparticles of fixed radius R, it is incorrect to compare quantitatively the calculated permittivity with the values measured in pressed nanopowders, the nanoparticles of which have a significant size spread, as well as likely different shapes.

To summarize, the size effect of the spontaneous polarization becomes significant for the average radius less than 10 nm and occurs near the FEI-AFE boundary. The size effect of the antipolar long-range order is significant near the reentrant FEI-FE transition boundary (for average radii 40÷50 nm).

3. Experimental Results

The details of the samples preparation and characterization is given in Ref. [3]. As-prepared $\mathrm{Bi}_{1-x}\mathrm{Sm}_x\mathrm{FeO}_3$ nanopowders were pressed in Polytetrafluoroethylene (PTFE) cells between two metallic plungers, which serve as electric contacts. The samples in the cell have a disk shape with the 6-mm diameter and (0.01÷0.05) mm thickness. All samples have the same thickness, much smaller than their 6-mm diameter, to avoid the influence of geometry effect on the measured capacitance and losses. The application of bigger pressure applied to thinner samples does not lead to any noticeable changes in their electrophysical properties, as well as the measured values were not changed after the pressure removal [3]; at that,

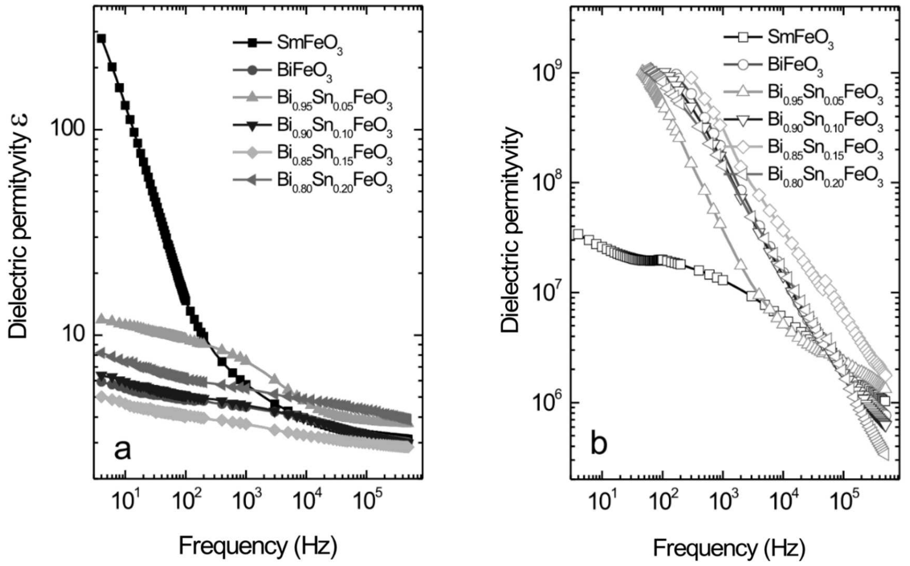

Fig. 2. Frequency dependence of the effective dielectric permittivity (*a*) and resistivity (*b*) measured for the pressed $Bi_{1-x}Sm_xFeO_3$ nanoparticles

the compression supports the stability of the powder sample during the I–V curves recording.

The RLC meters UNI-T UT612 and E7-12 were used to measure the capacitance of the cells in the range $(100-10^6)$ Hz. The electric voltage was applied to the sample connected in series with the load resistor from the software-controlled power supply GW Instek PSP-603.

Frequency dependence of the effective dielectric permittivity and resistivity of the pressed $Bi_{1-x}Sm_xFeO_3$ nanopowders are shown Fig. 2, *a* and Fig. 2, *b*, respectively.

From Fig. 2, *a*, the dielectric permittivity of the samples monotonically decreases with the frequency increase from 100 Hz to 1 MHz. The strongest decrease is observed for the pressed $SmFeO_3$ nanopowder, the weaker decrease is observed for the Sm content $x = 0.1$ and 0.15. The weakest decrease of the dielectric permittivity corresponds to the pressed $Bi_{0.8}Sm_{0.2}FeO_3$ nanopowders. The $(10{\div}1.5)$ times decrease in the dielectric permittivity under the frequency decrease over 4 decades is regarded the slow frequency dispersion characteristic for the wide-gap ferroelectric materials.

From Fig. 2, *b*, the resistivity of the pressed $Bi_{1-x}Sm_xFeO_3$ nanopowders very strongly and almost monotonically decreases with the frequency increase from 4 Hz to 1 MHz. The strongest decrease (by about 100 times) is observed for the pressed $SmFeO_3$ nanopowder, the weaker decrease is observed for the $BiFeO_3$ nanopowder. The resistivity of the pressed $SmFeO_3$ nanopowder are significantly lower than the losses of other samples in the frequency range at 4 Hz–1 kHz. It was shown [3] that the low resistivity of the pressed $SmFeO_3$ nanopowder is the reason of its dielectric permittivity increase at low frequences due to the interfacial barrier capacitance and/or Maxwell–Wagner type effects [34].

4. Conclusions

In this work, we have used the Ginzburg–Landau–Devonshire approach to perform phenomenological calculations of polar and dielectric properties of $Bi_{1-x}Sm_xFeO_3$ nanoparticles, and construct phase diagrams in dependence on the nanoparticle sizes and on the content of samarium in solid solution. Calculations of the surface adsorption/desorption influence on dielectric, polar, and magnetoelectric properties at different temperatures are performed in the framework of the Stephenson–Highland approach. The reentrant transition between the ferrielectric (FEI) and ferroelectric (FE) phases exists in the nanopowder with the average radius R of the $Bi_{1-x}Sm_xFeO_3$ nanoparticles, $R > R_R$. The influence of the average radius on the transition from the

FEI to the AFE phase is much weaker; and its influence on the AFE-NP transition is absent due to the absence of the depolarization field in the homogeneous AFE and NP phases [3]. The spontaneous polarization slightly depends on the average radius of $\mathrm{Bi}_{1-x}\mathrm{Sm}_x\mathrm{FeO}_3$ nanoparticles. It is maximal at $x = 0$, decreases monotonically with x increase and vanishes at $x \geq x_{\mathrm{cr}}(R)$, where $x_{\mathrm{cr}}(R) \approx 0.1$ for $R > 8$ nm. The spontaneous antipolar order exists in the FEI and AFE phases. It gradually disappears approaching the FEI-FE boundary and approaching the AFE-NP boundary, which is close to $x \approx 0.15$.

The dielectric permittivity diverges at the critical value $x = x_{\mathrm{cr}}$, where the critical Sm content x_{cr} increases with increase in the average radius of $\mathrm{Bi}_{1-x}\mathrm{Sm}_x\mathrm{FeO}_3$ nanoparticles. The divergency corresponds to the second order transition between the FEI and AFE phases [3]. The size effect of the spontaneous polarization becomes significant for the average radius less than 10 nm and occurs near the FEI-AFE boundary. The size effect of the antipolar long-range order is significant near the reentrant FEI-FE transition boundary (for radii $40 \div 50$ nm).

Experimental studies of the frequency dependence of the $\mathrm{Bi}_{1-x}\mathrm{Sm}_x\mathrm{FeO}_3$ nanopowders dielectric permittivity and resistivity a+re carried out. The results show that the strongest decrease is observed for the pressed SmFeO_3 nanopowder, the weakest decrease of the dielectric permittivity corresponds to the pressed $\mathrm{Bi}_{0.8}\mathrm{Sm}_{0.2}\mathrm{FeO}_3$ nanopowders. The decrease in the dielectric permittivity under the frequency decrease is related to the slow frequency dispersion characteristic for the wide-gap ferroelectric materials. The resistivity of the pressed $\mathrm{Bi}_{1-x}\mathrm{Sm}_x\mathrm{FeO}_3$ nanopowders decreases with the frequency increase from 4 Hz to 1 MHz. The strongest decrease is observed for the pressed SmFeO_3 nanopowder, the weaker decrease is observed for the BiFeO_3 nanopowder. The resistivity of the pressed SmFeO_3 nanopowder are significantly lower than the losses of other samples in the frequency range at 4 Hz–1 kHz.

Experimental results correlate with theoretical predictions, which allows one to improve the understanding of the physical mechanisms of conductivity and charge transfer in orthoferrite nanopowders, which will further allow us to create new nanocomposites with improved and/or controllable properties, as well as expand the perspectives of their advanced applications in nanoelectronics and energy storage.

Authors' contribution. *O.S.P. performed electrophysical measurements and analyzed results. V.O.K. and A.N.M. performed analytical calculations and prepared corresponding figures. I.V.F. prepared the samples and characterized them. V.N.P. and A.N.M. generated the research idea and formulated the problem.*

Authors dedicate the work to memory of Prof. Petro M. Tomchuk, who was a pioneer in theoretical research of the metal nanoparticles physical properties in our Institution. The work of O.S.P. and A.N.M. was funded by the National Research Foundation of Ukraine (project "Manyfold-degenerated metastable states of spontaneous polarization in nanoferroics: theory, experiment and perspectives for digital nanoelectronics", grant No. 2023.03/0132). V.O.K. and V.N.P. acknowledges the Target Program of the National Academy of Sciences of Ukraine, Project No. 5.8/25-P "Energy-saving and environmentally friendly nanoscale ferroics for the development of sensorics, nanoelectronics and spintronics".

APPENDIX A. Calculation details

The free energy of a homogeneous bulk $\mathrm{Bi}_{1-x}\mathrm{Sm}_x\mathrm{FeO}_3$ in the dimensionless form is as follows:

$$F_{\mathrm{bulk}} = \frac{1}{2}\alpha(T,x)P^2 + \frac{1}{2}\eta(T,x)A^2 + \\ + \frac{1}{4}\beta_{ij}\left(P_i^2P_j^2 + A_i^2A_j^2\right) + \frac{1}{2}\xi_{ij}P_i^2A_j^2 - \mathbf{PE}, \tag{A.1}$$

where $\alpha(T,x)$ пїS $\eta(T,x)$ – are dimensionless coefficients representing the linear stiffness of the sublattices. The dependences of these coefficients were obtained experimentally and are equal to:

$$\alpha(T,x) = \frac{T}{T_{\mathrm{C}}} - \exp\left[-\left(\frac{x}{x_c}\right)^4\right], \tag{A.2}$$

$$\eta(T,x) = \eta_0\left\{\frac{T}{T_A} - \exp\left[-\left(\frac{x}{x_A}\right)^2\right]\right\}, \tag{A.3}$$

where T – temperature, x – share of samarium in solid solution, T_{C} – Curie temperature, x_c is the proportion of samarium at which the phase transition from the ferroelectric (FE) phase to the nonpolar phase occurs, T_A is the Neel temperature, x_A is the proportion of samarium at which the phase transition from the antiferroelectric (AFE) phase to the nonpolar phase occurs, η_0 is a dimensionless coefficient corresponding to the relative amplitude of the AFE mode. $\mathbf{P} = (P_1, P_2, P_3)$ and $\mathbf{A} = (A_1, A_2A_3)$ are polar and antipolar dimensionless vectors, respectively, determined by the displacement vectors $\mathbf{C}_i$ ($i = 1, 2, 3, 4$) of the four sublattices:

$$\mathbf{P} = \frac{1}{2}\left(\mathbf{C}_1 + \mathbf{C}_2 + \mathbf{C}_3 + \mathbf{C}_4\right), \tag{A.4}$$

$$\mathbf{A} = \frac{1}{2}\left(\mathbf{C}_1 - \mathbf{C}_2 + \mathbf{C}_3 - \mathbf{C}_4\right). \qquad \text{(A.5)}$$

The lengths of the vectors are equal:

$$P^2 = P_1^2 + P_2^2 + P_3^2, \qquad \text{(A.6)}$$

$$A^2 = A_1^2 + A_2^2 + A_3^2. \qquad \text{(A.7)}$$

The coefficients $\beta_{ij} = \beta\delta_{ij}$ and $\xi_{ij} = \xi\delta_{ij}$ are used in the isotropic approximation, β is the nonlinearity coefficient, which is positive for the Landau expansion in even degrees up to the 4th, ξ is the interaction strength between sublattices, $\delta_{ij} = \begin{cases} 1, & i = j \\ 0, & i \neq j \end{cases}$ is the Kronecker delta. The gradient, elastic, and flexoelectric components for a homogeneous bulk undeformed volume of $\mathrm{Sm}_x\mathrm{Bi}_{1-x}\mathrm{FeO}_3$ can be neglected.

Sublattice equivalence can lead to the assumption $\beta_P = \beta_A = \beta = 1$ in Eq. (A.1) without loss of generality. The transition to dimensionless variables can be done in a scalar case as follows:

$$\tilde{F}_{\text{bulk}} \equiv \frac{F_{\text{bulk}}}{\alpha_0 P_0^2} = \frac{\alpha\,(T{,}x)}{2\alpha_0}\tilde{P}^2 + \frac{1}{2}\frac{\eta\,(T{,}x)}{\alpha_0}\tilde{A}^2 + $$
$$+ \frac{1}{4}\frac{\beta P_0^4}{\alpha_0 P_0^2}(\tilde{P}^4 + \tilde{A}^4) + \frac{\xi\,P_0^2}{2\alpha_0}\tilde{P}^2\tilde{A}^2 - \frac{\mathbf{PE}}{\alpha_0 P_0^2} = $$
$$= \frac{1}{2}\tilde{\alpha}\,(T{,}x)\,\tilde{P}^2 + \frac{1}{2}\tilde{\eta}\,(T{,}x)\,\tilde{A}^2 + \frac{1}{4}(\tilde{P}^4 + \tilde{A}^4) + $$
$$+ \frac{1}{2}\tilde{\xi}\tilde{P}^2\tilde{A}^2 - \tilde{\mathbf{P}}\tilde{\mathbf{E}}, \qquad \text{(A.8)}$$

where the dimensionless coefficients are:

$$\tilde{\alpha}\,(T, x) = \frac{\alpha\,(T, x)}{\alpha_0}, \tilde{\eta}\,(T, x) = \frac{\eta\,(T, x)}{\alpha_0}, \qquad \text{(A.9.1)}$$

$$\tilde{\xi} = \frac{\xi}{\beta}, \quad P_0^2 = \frac{\alpha_0}{\beta}, \quad \tilde{P}^2 = \frac{P^2}{P_0^2},$$
$$\tilde{A}^2 = \frac{A^2}{P_0^2}\,\tilde{E} = \frac{E}{\alpha_0 P_0}. \qquad \text{(A.9.2)}$$

The following formulas of the free energy contributions are valid:

$$F_{\text{bulk}} = \int\limits_V dV \left\{\frac{1}{2}\alpha P^2 + \frac{1}{2}\eta A^2 + \right.$$
$$\left. + \frac{1}{4}\beta_{ij}\left(P_i^2 P_j^2 + A_i^2 A_j^2\right) + \frac{1}{2}\xi_{ij} P_i^2 A_j^2\right\}, \qquad \text{(A.10)}$$

$$F_{\text{grad}} = \int\limits_V dV \frac{g_{ijkl}}{2}\left(\frac{\partial P_i}{\partial x_j}\frac{\partial P_k}{\partial x_i} + \frac{\partial A_i}{\partial x_j}\frac{\partial A_k}{\partial x_l}\right), \qquad \text{(A.11)}$$

$$F_{\text{el+fl}} = \int\limits_V dV \frac{F_{ijkl}}{2}\left\{\left(\frac{\partial P_i}{\partial x_j}\sigma_{kl} - \frac{\partial \sigma_{kl}}{\partial x_j}P_i\right) - \right.$$
$$\left. - \frac{s_{ijkl}}{2}\sigma_{ij}\sigma_{kl}\right\}, \qquad \text{(A.12)}$$

$$F_{el} = -\int\limits_V dV \left(P_i E_i + \frac{\varepsilon_0\varepsilon_b}{2}E^2\right), \qquad \text{(A.13)}$$

$$F_S = \frac{1}{2}\int\limits_S dS\left(c_p P^2 + c_A A^2\right), \qquad \text{(A.14)}$$

where: V is the volume, S is the area of the spherical nanoparticle $\mathrm{Bi}_{1-x}\mathrm{Sm}_x\mathrm{FeO}_3$, g_{ijkl} is the polarization gradient tensor, F_{ijkl} is the flexoelectric tensor, σ_{kl} are elastic stresses, s_{ijkl} are the components of the elastic compliance tensor, c_p and c_A are the surface energy coefficients, ε_0 is a universal dielectric constant, ε_b is the relative background permittivity, and E_i are the electric field components. We use the Einstein notation over the repeated subscripts i and/or j, where $i, j = 1$, 2, and 3.

The space-time evolution of polar and antipolar parameters of order P_i and A_i is determined from coupled time-dependent Euler–Lagrange equations obtained by minimizing the free energy F. These equations have the form:

$$\Gamma_{\text{p}}\frac{\partial P_i}{\partial t} + \alpha P_i + \beta_{ij}P_i P_j^2 + \xi_{ij}A_i^2 P_i - g_{ijkl}\frac{\partial P_k}{\partial x_j \partial x_l} = E_i, \qquad \text{(A.15)}$$

$$\Gamma_{\text{A}}\frac{\partial A_i}{\partial t} + \eta A_i + \beta_{ij}A_i A_j^2 + \xi_{ij}P_i^2 A_i - g_{ijkl}\frac{\partial A_k}{\partial x_j \partial x_l} = 0, \qquad \text{(A.16)}$$

where Γ_{p} and Γ_A are the Landau–Khalatnikov relaxation coefficients, the relaxation times P_i and A_i are $\tau_{\text{p}} = \Gamma_{\text{p}}/\left|a_p\right|$ and $\tau_{\text{A}} = \Gamma_{\text{A}}/\left|a_A\right|$, and no summation is performed over i.

Corresponding boundary conditions are:

$$\left.\left(c_p P_i - g_{ijkl}e_j\frac{\partial P_k}{\partial x_l}\right)\right|_S = 0, \qquad \text{(A.17a)}$$

$$\left.\left(c_a A_i - g_{ijkl}e_j\frac{\partial A_k}{\partial x_l}\right)\right|_S = 0, \qquad \text{(A.17b)}$$

where $\mathbf{e}$is the outer normal to the spherical surface of the nanoparticle S. $\Lambda_p = \frac{g}{c_p}$, $\Lambda_A = \frac{g}{c_A}$ are the extrapolation lengths (range 0.5–5 nm).

For simplicity, let us consider a single-domain spherical nanoparticle $\mathrm{Sm}_x\mathrm{Bi}_{1-x}\mathrm{FeO}_3$, in which the direction of spontaneous polarization $\mathbf{P}_s$ is collinear with the 3-rd axis. For the geometry, the electric field component is the superposition of the external and depolarization fields E_3^e and E_3^d respectively. For a single-domain nanoparticle, the analytical expressions for the electric field components are as follows:

$$E_3^d = \frac{n_d}{\varepsilon_b n_d + \varepsilon_M\left(1 - n_d\right) + \varepsilon_s n_d\left(D/\lambda\right)}\frac{P_3}{\varepsilon_0}, \qquad \text{(A.18)}$$

$$E_3^e = \frac{\varepsilon_M}{\varepsilon_b n_d + \varepsilon_M\left(1 - n_d\right) + \varepsilon_s n_d\left(D/\lambda\right)}E_3^0. \qquad \text{(A.19)}$$

Here D is the ellipsoid semi-axis (R or L) in the direction of spontaneous polarization P_3, λ is the effective shielding length, ε_s is the relative permittivity, and $\varepsilon_M$is the relative effective permittivity of the medium.

1. F. Zhang, X. Zeng, D. Bi, K. Guo, Y. Yao, S. Lu. Dielectric, Ferroelectric, and magnetic properties of SM-doped bifeo3 ceramics prepared by a modified solid-state-reaction method. *Materials* **11** (11), 2208 (2018).
2. W. Yan, Z.-L. Hou, S. Bi, R.-B. Cui, M. Tang. Enhanced magnetization and bias voltage-dependent dielectric properties of SM-doped bifeo3 multiferroic nanofibers. *J. Mater. Sci.* **53** (14), 10249 (2018).
3. A.N. Morozovska, E.A. Eliseev, I.V. Fesych, Y.O. Zagorodniy, O.S. Pylypchuk, E.V. Leonenko *et al.* Reentrant polar phase induced by the ferro-ionic coupling in

$Bi_{1-x}Sm_xFeO_3$ nanoparticles. *Phys. Rev. B* **110**, 224110 (2024),

4. S. Chaturvedi, S.K. Singh, P. Shyam, M.M. Shirolkar, S. Krishna, R. Boomishankar *et al.* Nanoscale $LuFeO_3$: Shape dependent ortho/hexa-phase constitution and nanogenerator application. *Nanoscale* **10** (45), 21406 (2018).
5. Z. Fan, S. Gao, Y. Chang, D. Wang, X. Zhang, H. Huang *et al.* Ultra-superior high-temperature energy storage properties in polymer nanocomposites via rational design of core–shell structured inorganic antiferroelectric fillers. *J. Mater. Chem. A* **11** (13), 7227 (2023).
6. L. Baudry, I. Lukyanchuk, V.M. Vinokur. Ferroelectric symmetry-protected multibit memory cell. *Sci. Rep.* **7**, 42196 (2017).
7. C. Anthonyraj, M. Muneeswaran, S. Gokul Raj, N.V. Giridharan, V. Sivakumar, G. Senguttuvan. Effect of samarium doping on the structural, optical and magnetic properties of sol–gel processed $BiFeO_3$ thin films. *J. Mater. Sci.: Mater. Electron.* **26** (1), 49 (2014).
8. H. Singh, K.L. Yadav. Structural, dielectric, vibrational and magnetic properties of SM doped $BiFeO_3$ multiferroic ceramics prepared by a rapid liquid phase sintering method. *Ceramics International* **41** (8), 9285 (2015).
9. V.A. Khomchenko, D.V. Karpinsky, M.V. Bushinsky, D.V. Zhaludkevich, A. Franz, M.V. Silibin. Effect of Mn substitution on the crystal and magnetic structure of $Bi_{1-x}Ca_xFeO_{3-x/2}$ multiferroics. *Mater. Lett.* **266**, 127470 (2020).
10. A. Haruna, I. Abdulkadir, S.O. Idris. Photocatalytic activity and doping effects of $BiFeO_3$ nanoparticles in model organic dyes. *Heliyon* **6** (1), e03237 (2020).
11. T. Zheng, J. Wu. Effects of site engineering and doped element types on piezoelectric and dielectric properties of bismuth ferrite lead-free ceramics. *J. Mater. Chem. C* **3** (43), 11326 (2015).
12. H.H. Singh, H.B. Sharma. Enhanced Electrical and magnetic properties of samarium (SM) doped multiferroic bismuth ferrite (BFO) ceramics. *Integrated Ferroelectrics*, **203** (1), 120 (2019).
13. S. Irfan, Y. Shen, S. Rizwan, H. Wang, S.B. Khan, C. Nan. Band-gap engineering and enhanced photocatalytic activity of Sm and Mn doped $BiFeO_3$ nanoparticles. *J. American Ceramic Society* **100** (1), 31 (2016).
14. Y.B. Yao, W.C. Liu, C.L. Mak. Pyroelectric properties and electrical conductivity in samarium doped $BiFeO_3$ ceramics. *J. Alloys and Compounds* **527**, 157 (2012).
15. Md.S. Sheikh, T.K. Bhowmik, A. Dutta, S. Saha, C.R. Joshi, T.P. Sinha. Triclinic $BiFeO_3$: A room-temperature multiferroic phase with enhanced magnetism and resistivity. *Phys. Rev. B* **108** (10), 104427 (2023).
16. Y.-W. Lu, X. Qi. Hydrothermal synthesis of pure and SB-doped $BiFeO_3$ with the typical hysteresis loops of ideal ferroelectrics. *J. Alloys and Compounds* **774**, 386 (2019).
17. K.Y. Yun, M. Noda, M. Okuyama. Prominent ferroelectricity of $BiFeO_3$ thin films prepared by pulsed-laser deposition. *Appl. Phys. Lett.* **83** (19), 3981 (2003).
18. W. Eerenstein, N.D. Mathur, J.F. Scott. Multiferroic and magnetoelectric materials. *Nature* **442** (7104), 759 (2006).
19. R. Ramesh. Emerging routes to multiferroics. *Nature* **461** (7268), 1218 (2009).
20. S.-W. Cheong, M. Mostovoy. Multiferroics: A magnetic twist for ferroelectricity. *Nature Materials* **6** (1), 13 (2007).
21. G. Catalan, J.F. Scott. Physics and applications of bismuth ferrite. *Advanced Materials* **21** (24), 2463 (2009).
22. M. Fiebig. Revival of the magnetoelectric effect. *J. Phys. D: Appl. Phys.* **38** (8), R123 (2005).
23. I.V. Blonskii, E.A. Eliseev, P.M. Tomchuk. Abstract the photogeneration of sound by the ensemble of nanoclusters incorporated in a dielectric matrix. *Ukr. J. Phys.* **45** (9), 1110 (2000).
24. P.M. Tomchuk, D.V. Butenko. The nanoparticle shape's effect on the light scattering cross-section. *Surf. Sci.* **606**, 1892 (2012).
25. P.M. Tomchuk, Y. Bilotsky. New peculiarity in the temperature and size dependence of electron-lattice energy exchange in metal nanoparticles. *Int. J. Mod. Phys. B* **28**, 1450220 (2014).
26. P.M. Tomchuk, D. Butenko. Nonlocal effects in metallic nanoparticles: The kinetic approach outlook. *Int. J. Mod. Phys. B* **31**, 1750029 (2017).
27. A.N. Morozovska, E.A. Eliseev, S.V. Kalinin, Y.M. Vysochanskii, P. Maksymovych. Stress-induced phase transitions in nanoscale. *Phys. Rev. B* **104** (5), 054102 (2021).
28. A.K. Tagantsev, G. Gerra. Interface-induced phenomena in polarization response of ferroelectric thin films. *J. Appl. Phys.* **100** (5), 051607 (2006).
29. L.D. Landau, E.M. Lifshitz, L.P. Pitaevskii. *Electrodynamics of Continuous Media* (Butterworth-Heinemann, 1984).
30. E.A. Eliseev, A.V. Semchenko, Y.M. Fomichov, M.D. Glinchuk, V.V. Sidsky, V.V. Kolos, Yu.M. Pleskachevsky, M.V. Silibin, N.V. Morozovsky, A.N. Morozovska. Surface and finite size effects impact on the phase diagrams, polar, and dielectric properties of (Sr, Bi)Ta_2O_9 ferroelectric nanoparticles. *J. Appl. Phys.* **119** (20), 204104 (2016).
31. A.N. Morozovska, M.D. Glinchuk, E.A. Eliseev. Phase transitions induced by confinement of ferroic nanoparticles. *Phys. Rev. B* **76** (1), 014102 (2007).
32. A.N. Morozovska, I.S. Golovina, S.V. Lemishko, A.A. Andriiko, S.A. Khainakov, E.A. Eliseev. Effect of Vegard strains on the extrinsic size effects in ferroelectric nanoparticles. *Phys. Rev. B* **90** (21), 214103 (2014).
33. A.N. Morozovska, Y.M. Fomichov, P. Maksymovych, Y.M. Vysochanskii, E.A. Eliseev. Analytical description of domain morphology and phase diagrams of ferroelectric nanoparticles. *Acta Materialia* **160**, 109 (2018).
34. K.W. Wagner. Erklärung der dielektrischen Nachwirkungsvorgänge auf Grund Maxwellscher Vorstellungen. *Arch Elektrotech.* **2**, 371 (1914).

Received 08.07.25

О.С. Пилипчук, В.О. Колупаєв,
І.В. Фесич, В.М. Порошин, Г.М. Морозовська

ДОСЛІДЖЕННЯ ЕЛЕКТРОФІЗИЧНИХ ВЛАСТИВОСТЕЙ, ФАЗОВИХ ДІАГРАМ ТА ПЕРЕНОСУ НОСІЇВ ЗАРЯДУ В НАНОПОРОШКАХ $\mathrm{Bi}_{1-x}\mathrm{Sm}_x\mathrm{FeO}_3$

Нанорозмірні мультифероїки з різними параметрами розмірів і форми є базовими модельними об'єктами для вивчення полярної, антиполярної та магнітної орієнтації, а також магнітоелектричної взаємодії. Оксид вісмуту-самарію ($\mathrm{Bi}_{1-x}\mathrm{Sm}_x\mathrm{FeO}_3$) є класичним ортоферитом, полярні та магнітні властивості якого достатньо вивчені як для об'ємних зразків, так і для тонких плівок. Однак властивості саме наночастинок $\mathrm{Bi}_{1-x}\mathrm{Sm}_x\mathrm{FeO}_3$ вивчені набагато менше теоретично та експериментально, не дивлячись на те, що вони можуть бути використані для збору та зберігання енергії, а також для створення сучасних комірок енегонезалежної фероелектричної пам'яті. У цій роботі ми застосували метод Гінзбурга–Ландау–Девоншира для проведення феноменологічних розрахунків полярних і діелектричних властивостей наночастинок $\mathrm{Bi}_{1-x}\mathrm{Sm}_x\mathrm{FeO}_3$ і побудови фазових діаграм залежно від середнього розміру наночастинок, а також від частки самарію в твердому розчині. Вплив поверхневої адсорбції/десорбції на діелектричні, полярні та магнітоелектричні властивості за різних температур розраховано з використанням підходу Стефенсона–Хайленда. Проведено експериментальні дослідження частотної залежності діелектричної сприйнятливості та провідності нанопорошків $\mathrm{Bi}_{1-x}\mathrm{Sm}_x\mathrm{FeO}_3$. Результати експериментальних досліджень корелюють з теоретичними передбаченнями, що в сукупності поглиблює розуміння фізичних механізмів провідності та переносу заряду в нанопорошках ортофериту, що в подальшому дасть змогу створювати нові нанокомпозити з покращеними та/або керованими властивостями, а також розширить перспективи їх активного застосування в наноелектроніці та накопичувачах енергії.

Ключові слова: діелектрична проникність, питомий опір, ортоферит, наночастинки, мультифероїк, електрофізичні властивості, фазовий перехід, фазова діаграма.